Flow Turbulence Combust (2010) 85:279–307
DOI 10.1007/s10494-010-9292-1

Large-Eddy Simulation for an Axisymmetric Piston-Cylinder Assembly With and Without Swirl

Kai Liu · D. C. Haworth

Received: 16 November 2009 / Accepted: 19 August 2010 / Published online: 14 September 2010

Abstract Large-eddy simulation (LES) has been performed for an axisymmetric piston-cylinder assembly with and without swirl. For both cases, the LES mean and rms velocity profiles show better agreement with experimental data than profiles obtained using a Reynolds-averaged Navier–Stokes (RANS) approach with a standard $k - \varepsilon$ turbulence model. The sum of the resolved and modeled contributions to turbulence kinetic energy (TKE) approaches grid independence for the meshes used in this study. The sensitivity of LES to key numerical and physical model parameters has been investigated. Results are especially sensitive to mesh and to the subfilter-scale (SFS) turbulence models. Satisfactory results can be obtained using simple viscosity-based SFS turbulence models, although there is room for improvement. No single model gives uniformly best agreement between model and measurements at all spatial locations and at all times. The strong sensitivity of computed mean and rms velocity profiles to variations in the SFS turbulence model suggests that better results might be obtained using more sophisticated models.

Keywords Turbulence · Large-eddy simulation · IC engine

K. Liu (✉)
Department of Mechanical and Nuclear Engineering,
The Pennsylvania State University,
224 Research Building East, University Park, PA 16802, USA
e-mail: kailiu@psu.edu

D. C. Haworth
Department of Mechanical and Nuclear Engineering,
The Pennsylvania State University,
232 Research Building East, University Park, PA 16802, USA
e-mail: dch12@psu.edu

1 Introduction

Large-eddy simulation (LES) is increasingly used as a tool for studying the dynamics of turbulence in engineering flows. In LES, one explicitly captures the dynamics of the large eddies while modeling the effects of the smaller eddies on the larger ones. Because the statistics of small-scale turbulence are expected to be more universal than those of the large scales, LES offers the promise of wider generality and more accurate results compared to Reynolds-averaged Navier–Stokes (RANS) where the effects of all turbulence scales are modeled, while requiring smaller computational resources compared with direct numerical simulation (DNS) where all turbulence scales are resolved.

In RANS for in-cylinder flow in a reciprocating-piston internal combustion (IC) engine, the local instantaneous value of a computed variable represents an ensemble- or phase-average over many engine cycles at a specified spatial location and crank phasing. The shortcomings of RANS models have been argued by many turbulence researchers, and discussions of engine-specific issues can be found in [1–3] and [4], for example. In contrast to RANS, in LES one solves the spatially filtered Navier–Stokes equations. It has long been argued that turbulence modeling based on spatial filtering offers advantages compared to time- or phase-averaging [5], and these advantages are particularly compelling for the IC-engine application [1–4]. For example, cycle-to-cycle flow and combustion variability, which are not accessible from RANS, can be captured in principle.

There are important differences between RANS and LES [3]. A consistent RANS methodology converges to an exact solution of the Reynolds-averaged Navier–Stokes equations with increasing spatial and temporal resolution. Thus the numerical accuracy can be improved, but the dynamic range of scales that is resolved can not be increased with grid refinement. In LES where the filter width Δ is independent of mesh size, similar convergence to an exact solution of the spatially filtered governing equations can be realized. It is more often the case in LES that the filter width Δ is proportional to the mesh size. In that case the dynamic range of scales that is resolved will increase with increasing spatial and temporal resolution, and a consistent LES may converge to an exact solution of the unfiltered Navier–Stokes equations: that is, to DNS. Usually grid independence in LES can be established only in a statistical sense; the sum of resolved and subfilter-scale contributions to mean quantities should be independent of numerical parameters such as mesh size and computational time step, for example.

Since LES can better capture the details of the turbulence dynamics including cycle-to-cycle variations, the transition of in-cylinder CFD from RANS to LES is a natural direction. El Tahry and Haworth [1] argued in 1992 that the computational meshes typically used for RANS modeling of practical in-cylinder configurations should be sufficient to capture 80–90% of the flow's kinetic energy. For IC engines at moderate Reynolds numbers, it has been estimated that grid independent (to within 10–20%) profiles of dependent mean variables in RANS computations of in-cylinder flow and combustion would require at least 10^6 mesh points using second-order or higher numerical methods [2]. This corresponds to sub-millimeter mesh spacing in a typical automotive IC engine, and it is not far beyond current RANS practice. Other arguments for pursuing LES for in-cylinder CFD have been made in [4] and [6]. Even if comparable meshes are used, LES will require more computational effort

compared with RANS, because smaller computational time steps may be required and simulations may need to be carried through multiple engine cycles.

Over the last twenty years, significant progress has been made in LES for IC engines. El Tahry and Haworth [1] argued that LES would be the direction for the next-generation turbulence models that have potential for significant improvement over RANS. Early LES applications in IC engines were reviewed by Celik, Yavuz and Smirnov in [7]. Haworth and Jansen [2] reported encouraging results using LES for predicting the ensemble-averaged mean and rms velocity profiles for a simplified motored engine configuration. Naitoh et al. [8] performed LES for turbulent premixed-flame propagation in IC engines on relatively coarse grids. Celik et al. [9, 10] applied LES to a realistic engine geometry under motored conditions to predict turbulent fluctuations and statistics using KIVA [11]. Smirnov et al. [12, 13] also applied LES in KIVA for fuel injection and combustion in diesel engines. Richard et al. [14] modified RANS spark-ignition and flame-propagation models for LES and reported model validation for a nonengine configuration and a single-cycle engine; Vermorel et al. [15] then simulated nine consecutive complete engine cycles for a single cylinder, spark-ignited four-valve engine. Other recent examples include Goryntsev et al. [16] (cycle-to-cycle variations of mixture preparation in a direct-injection gasoline engine) and Banerjee et al. [17] (LES for a direct-injection diesel engine). The level of activity and number of publications have increased dramatically in recent years. A dedicated conference was orgnized in late 2008 [18], and another is planned for late 2010. Although LES has been applied to realistic engine configurations, there is still much that can be learned from modeling simple configurations about the behavior of the subfilter-scale (SFS) models and numerical algorithms.

This research addresses important outstanding issues for in-cylinder LES in the context of a simplified engine-like configuration. These includes systematic comparisons between a conventional two-equation RANS model and LES; a systematic parametric study of the effects of physical model parameters and numerical parameters; quantification of the quality of the LES solutions through an examination of the relative magnitudes of resolved-scale and subfilter-scale fluctuations; and the first LES results reported to date for a model engine configuration with swirl.

The remainder of this paper is organized as follows. In Section 2, the experimental configurations are described. In Section 3, the mathematical formulations, physical models and numerical methods are introduced. The results are presented in Section 4, and conclusions are drawn in Section 5.

2 Experimental Configurations

The axisymmetric piston-cylinder assembly that is the subject of this study is shown schematically in Fig. 1; key geometric parameters and operating conditions are also summarized there [19]. This is a pancake (flat head and piston) chamber with a 75-mm bore, 60-mm stroke, and 30-mm clearance. The piston moves in simple harmonic motion at a crankshaft rotational speed of $\Omega_{CS} = 200$ rpm (mean piston speed $\overline{V_p} = 0.4$ m/s). Flow enters the chamber through an annular passage angled at 30° with respect to the cylinder axis through a fixed, open valve. For the swirling cases, swirl vanes are added upstream of the valve around the valve stem. The angle

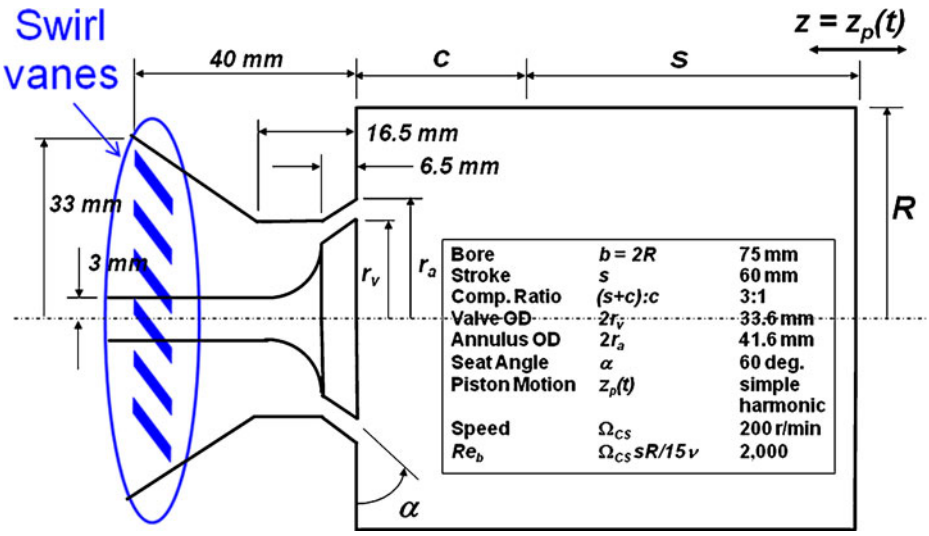

Fig. 1 Axisymmetric piston-cylinder assembly [19]

of the valve entry is 30° with respect to the cylinder axis and the width of the parallel section is 4 mm, measured in the radial direction [20, 21]. The working fluid is air, which is treated as an ideal gas. The ambient pressure and temperature are taken to be uniform at 1 atm and 300 K, respectively.

For both swirling and nonswirling cases, Laser–Doppler anemometry has been used to obtain ensemble- (phase-) averaged radial profiles of mean and rms velocity components at 10-mm axial increments starting from the head for crank positions of 36°, 90° and 144° after piston top-dead-center (TDC) [19–22]. For nonswirling cases, only the axial velocity component was measured and measurements also were reported at 270° after TDC. For the swirling case, mean and rms profiles of all three velocity components (axial, radial, and tangential) were reported. The number of samples (engine cycles) was 100, and five sets of data were taken to confirm repeatability.

Sources of experimental error include uncertainty in the position of measurement, flow asymmetry, variation in the speed of the engine and the rotating diffraction grating, velocity-gradient broadening, crank-angle broadening and biasing effects due to limited amplifier bandwidth and filter setting. The uncertainties are discussed in detail in [20, 21]; there it was concluded that the uncertainty in the mean velocity values does not exceed 3%, except at the lowest mean velocities and highest rms levels. Further confirmation was provided by evaluating the net mass flow rates from the measured velocity profiles.

The nonswirling case has been the subject of numerous RANS-based (reviewed in [1]) and LES-based [2, 3, 23] modeling studies. The swirling case is more complex: RANS-based calculations have been performed by El Tahry [24] using three different turbulence models, and no LES results have been reported to date. Here a comprehensive LES study is reported for both swirling and nonswirling cases with systematic variations in numerical parameters and physical models.

3 Mathematical Formulation, Physical Models and Numerical Methods

3.1 Governing equations

In LES, one uses a low-pass spatial filter to eliminate the dynamics of scales smaller than a selected filter width Δ from the instantaneous Navier–Stokes equations. Subfilter-scale models then are introduced to account for the effects of the unresolved scales. In general, the filter width Δ should be smaller than the size of the smallest energy-containing eddies; ideally, Δ should lie in the inertial subrange. Further details can be found in [25], for example.

The starting point is the instantaneous Navier–Stokes equations:

$$\frac{\partial}{\partial t}(\rho u_i) + \frac{\partial}{\partial x_j}(\rho u_i u_j) = -\frac{\partial p}{\partial x_i} + \frac{\partial \sigma_{ij}}{\partial x_j}, \tag{1}$$

where ρ is the density, u_i is the velocity component in the i-direction, p is the pressure, and σ_{ij} is the viscous stress tensor. A spatial filter is applied, and each quantity is decomposed into the sum of a spatially filtered contribution (denoted using an overbar) and a fluctuation about the spatially filtered value (denoted using a prime). For example,

$$u_i = \bar{u}_i + u_i'. \tag{2}$$

The resulting filtered Navier–Stokes equations can be written as:

$$\frac{\partial}{\partial t}(\bar{\rho}\widetilde{u}_i) + \frac{\partial}{\partial x_j}(\bar{\rho}\widetilde{u}_i\widetilde{u}_j + \bar{p}\delta_{ij}) = \frac{\partial}{\partial x_j}(\bar{\sigma}_{ij} + \tau_{\mathrm{SFS},ij}), \tag{3}$$

where '$\sim$' denotes a density-weighted (Favre) filtered value:

$$\widetilde{u}_i \equiv \overline{\rho u}_i / \bar{\rho}. \tag{4}$$

The quantity $\tau_{\mathrm{SFS},ij} = \bar{\rho}(\widetilde{u_i u_j} - \widetilde{u_i}\widetilde{u_j})$ is an apparent subfilter-scale stress [25–27]. Here the SFS stress is modeled using eddy-viscosity type closures, which assume a linear relationship between the SFS stresses and the resolved rate-of-strain, $\widetilde{S}_{ij} = \frac{1}{2}(\partial\widetilde{u}_i/\partial x_j + \partial\widetilde{u}_j/\partial x_i)$ [27]:

$$\tau_{\mathrm{SFS},ij} = 2\mu_{\mathrm{SFS}}\widetilde{S}_{ij} - \frac{2}{3}\bar{\rho}k_{\mathrm{SFS}}\delta_{ij} - \frac{2}{3}\mu_{\mathrm{SFS}}\frac{\partial\widetilde{u}_k}{\partial x_k}\delta_{ij}, \tag{5}$$

where k_{SFS} is the SFS turbulent kinetic energy defined as:

$$\bar{\rho}k_{\mathrm{SFS}} = -\frac{1}{2}\tau_{\mathrm{SFS},kk}, \tag{6}$$

and μ_{SFS} is an apparent SFS turbulent viscosity.

3.2 Subfilter-scale models

Many SFS models have been proposed to model the influence of unresolved (subfilter-scale) motions on resolved scales. Two SFS models are considered here: a Smagorinsky SFS model, and a one-equation SFS model.

3.2.1 Smagorinsky model

The Smagorinsky model is the most commonly used SFS model [28]. It is derived from a local equilibrium assumption: the production and dissipation of SFS turbulent kinetic energy are equal. It can be written in the following form [28]:

$$\mu_{\mathrm{SFS}} = \bar{\rho} C_s \Delta^2 2^{1/2} \|\underline{\widetilde{S}}\|, \tag{7}$$

where $\|\underline{\widetilde{S}}\| = (\widetilde{S}_{ij}\widetilde{S}_{ij})^{1/2}$ is the Frobenius norm of the resolved strain-rate tensor, and Δ is taken as $V_{\mathrm{cell}}^{1/3}$ [29], where V_{cell} is the volume of a computational cell. The baseline value of the model constant C_s is taken to be the square of the classic Smagorinsky constant ($C_s = 0.165^2$) [30, 31] and the values can be adjusted following the recommendations available in the literature for shear flows and free flows [32, 33]. The SFS kinetic energy then is modeled using a closure similar to the one proposed by Yoshizawa [34]:

$$k_{\mathrm{SFS}} = 2 C_I \Delta^2 \|\underline{\widetilde{S}}\|^2. \tag{8}$$

The standard value of the model constant C_I is 0.202. The subfilter-scale turbulent dissipation rate $\varepsilon_{\mathrm{SFS}}$ then can be defined as:

$$\varepsilon_{\mathrm{SFS}} = 2 C_\varepsilon \frac{k_{\mathrm{SFS}}^{3/2}}{\Delta}, \tag{9}$$

where C_ε can be obtained from equilibrium arguments as:

$$C_\varepsilon = 2 C_s C_I^{-3/2}. \tag{10}$$

3.2.2 One-equation model

Speziale [35] recommended solving a transport equation for k_{SFS} rather than using a local equilibrium assumption for the SFS kinetic energy. A modeled transport equation for k_{SFS} can be written as,

$$\frac{\partial \bar{\rho} k_{\mathrm{SFS}}}{\partial t} + \frac{\partial \bar{\rho} \widetilde{u}_j k_{\mathrm{SFS}}}{\partial x_j} = -\tau_{\mathrm{SFS},ij}\widetilde{S}_{ij} - C_1 \bar{\rho} \frac{k_{\mathrm{SFS}}^{3/2}}{\Delta} + \frac{\partial}{\partial x_j}\left[C_k \bar{\rho} \Delta k_{\mathrm{SFS}}^{1/2} \frac{\partial k_{\mathrm{SFS}}}{\partial x_j} \right]. \tag{11}$$

Here the standard value for model constants C_1 and C_k are: $C_1 = 1.0$ and $C_k = 0.05$. The turbulent kinetic energy thus obtained is then used as a velocity scale for the SFS viscosity [34, 36, 37]:

$$\mu_{\mathrm{SFS}} = C_k \bar{\rho} \Delta k_{\mathrm{SFS}}^{1/2}. \tag{12}$$

3.2.3 Wall models

For wall-bounded flows, most turbulence is generated in the near-wall region. It is therefore necessary to resolve the details of the near-wall flow, which requires a fine mesh. A wall model can be used to model the turbulence in the near-wall region to relax the mesh-resolution requirements. Here the near-wall treatment is implemented as a two-step process. In the first step, the wall friction velocity u_τ is estimated by inverting a third-order Spalding law [38]:

$$y^+ = u^+ + \frac{1}{E}\left(e^{\kappa u^+} - 1 - \kappa u^+ - \frac{(\kappa u^+)^2}{2} - \frac{(\kappa u^+)^3}{3!} \right), \tag{13}$$

where y^+ and u^+ are obtained from:

$$y^+ = yu_\tau/\nu, \tag{14}$$

$$u^+ = u/u_\tau, \tag{15}$$

$$u_\tau = (\tau_w/\rho)^{1/2}. \tag{16}$$

Here y is the wall-normal distance, $\nu = \mu/\rho$ is the kinematic viscosity, and τ_w is the wall shear stress. The empirical constants κ and E are equal to 0.41 and 9.00, respectively, for a smooth wall. In the second step, the relevant fluxes for momentum, thermal energy and chemical species are computed on the basis of an estimated u_τ. The wall models are active only in those cells that have one or more faces that correspond to a wall, following standard practice.

3.3 Numerical methods

The CFD code STAR-CD version 4.06 [39] has been used for this study. Second-order central differencing is used for the convective terms in the momentum equation, and the PISO algorithm [40] with implicit time differencing is used for pressure-velocity coupling. This has been shown to yield approximately second-order time accuracy. Values of the numerical parameters recommended for LES applications are provided in [39, 41].

3.4 Computational mesh

The mesh topology is illustrated in Fig. 2. An unstructured mesh has been used to maintain approximately uniform mesh spacing in the in-cylinder region. All cells are hexahedral, including the region around the valve. The total number of computational cells including the valve region is 168,880 for the coarse mesh shown in Fig. 2. Two different ways of moving the mesh to accommodate piston motion

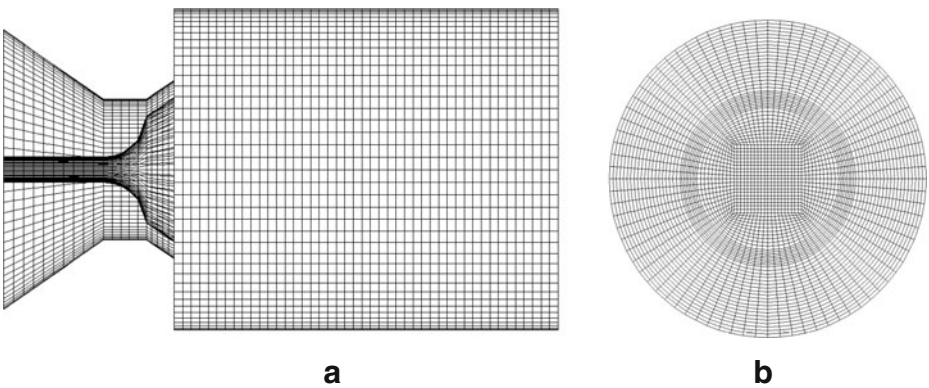

Fig. 2 2-D sections through the computational mesh for the axisymmetric piston-cylinder assembly. **a** Cross section containing the axis of symmetry. **b** Cross section normal to the axis of symmetry

were explored. The first approach is to deform the mesh without cell removal or addition. In that case, the aspect ratio of in-cylinder cells varies by a factor of three over a cycle. The second approach is to remove and add mesh layers in the cylinder. In that case, the aspect ratios of in-cylinder cells remain constant, except for the layer of cells adjacent to the piston. The number of in-cylinder cells varies by a factor of three over an engine cycle. Both approaches have been implemented in this study, and a comparison of the two approaches is made in Section 4.1.

A similar mesh size and topology was used in the early LES study of Haworth and Jansen [2]. There the total mesh size was 151,620 cells. This is rather coarse by modern standards. The baseline mesh for the present study contains approximately 1.3 million cells, and corresponds to a factor of two mesh refinement in each direction with respect to the coarse mesh shown in Fig. 2. A fine mesh of approximately 2.6 million cells (additional factor of two mesh refinement in the axial direction only) also was tested. The number of cells in the radial direction in the annular valve gap is 8 for the coarse mesh and 16 for the baseline and fine meshes.

3.5 Initial and boundary conditions and the estimation of mean quantities

For the Imperial College piston-cylinder assembly, the initial pressure and temperature are uniform at 1 atm and 300 K, respectively. The no-slip boundary condition is applied at solid walls, and all walls are adiabatic. There is a large plenum upstream of the valve (not shown in Fig. 2) so that no inflow-outflow boundary conditions are needed. The volume of the plenum is approximately 50 times larger than that of the in-cylinder region, so that the global pressure and temperature vary less than 2% through each engine cycle.

The computations begin at bottom-dead-center (BDC). For nonswirling cases, the simulations are run through seven engine cycles, and the first two cycles are discarded to avoid contamination by initial conditions. Sensitivity of results to the number of cycles is discussed in Section 4.1. In general, one would expect five cycles to be too few to compile converged ensemble-averaged point statistics. However, we take advantage of the statistical axisymmetry of the configuration to extract meaningful averages. At a specified crank-angle position (time) and axial location, radial profiles of velocity are sampled at 20° azimuthal increments around the cylinder axis, yielding 18 profiles that can be averaged from each engine cycle. The effective number of samples is then 18 times the number of cycles simulated; for five cycles, this is close to the 100 samples that were taken in the experiments. Standard scaling arguments suggest [2] that the turbulence integral length scale at TDC should be equal to a fraction of the clearance height; in the annular jet during induction, the turbulence integral length scale should be proportional to the annulus width. Together, these suggest an upper bound on the turbulence integral scale of approximately 4∼5 mm. The 20° sampling angle corresponds to an azimuthal separation of at least 4 mm as close as 11 mm to the cylinder axis. At smaller radial distances, the 18 samples may not be statistically independent, yielding increasing statistical uncertainty in the computed averages as we approach the axis of symmetry.

For the swirling case, the simulations were run for ten cycles and the first five cycles were discarded. A rotating body force was added in the momentum equation in the region upstream of intake valve to mimic the effect of swirl vanes. The magnitude of the body force was adjusted to give the correct global level of in-cylinder swirl.

3.6 A two-equation RANS turbulence model

It is appropriate to compare the LES results with results from a standard RANS-based turbulence model that typically would be used for IC engines. A two-equation $k-\varepsilon$ model suffices for this purpose. In that case, modeled equations are solved for turbulence kinetic energy, k, and the viscous dissipation rate of turbulence kinetic energy, ε. The equations are:

$$\frac{\partial}{\partial t}(\langle\rho\rangle k)+\frac{\partial}{\partial x_j}\left[\langle\rho\rangle\widehat{u}_j k-\left(\mu+\frac{\mu_t}{\sigma_k}\right)\frac{\partial k}{\partial x_j}\right]=\mu_t P-\rho\varepsilon-\frac{2}{3}\left(\mu_t\frac{\partial\widehat{u}_i}{\partial x_i}+\langle\rho\rangle k\right)\frac{\partial\widehat{u}_i}{\partial x_i}, \tag{17}$$

where '$\langle\rangle$' denotes an ensemble-averaged value, '$\wedge$' denotes a Favre-averaged (density-weighted mean) value, P is the turbulence production rate,

$$P\equiv\widehat{S}_{ij}\frac{\partial\widehat{u}_i}{\partial x_j}, \tag{18}$$

and,

$$\frac{\partial}{\partial t}(\langle\rho\rangle\varepsilon)+\frac{\partial}{\partial x_j}\left[\langle\rho\rangle\widehat{u}_j\varepsilon-\left(\mu+\frac{\mu_t}{\sigma_\varepsilon}\right)\frac{\partial\varepsilon}{\partial x_j}\right]=C_{\varepsilon1}\frac{\varepsilon}{k}\left[\mu_t P-\frac{2}{3}\left(\mu_t\frac{\partial\widehat{u}_i}{\partial x_i}+\langle\rho\rangle k\right)\frac{\partial\widehat{u}_i}{\partial x_i}\right]$$
$$-C_{\varepsilon2}\langle\rho\rangle\frac{\varepsilon^2}{k}+C_{\varepsilon3}\langle\rho\rangle\varepsilon\frac{\partial\widehat{u}_i}{\partial x_i}. \tag{19}$$

The turbulence viscosity in the mean momentum equation then is specified as,

$$\mu_t=\frac{C_\mu\rho k^2}{\varepsilon}. \tag{20}$$

Here σ_k, σ_ε, C_μ, $C_{\varepsilon1}$,$C_{\varepsilon2}$ and $C_{\varepsilon3}$ are model constants; standard values are given in Table 1 [42–44]. The mean dilatation term in (19) was introduced by El Tahry [44]; there the value $C_{\varepsilon3}=-1/3$ was deduced analytically with an assumption of local isotropy.

Standard wall functions are applied to the cells immediately adjacent to walls [39, 42, 45]. The wall-function approach uses algebraic relations to model the distributions of velocity, temperature, and turbulence parameters across the boundary layer when the centroid of a near-wall cell lies in the logarithmic region of the boundary layer [39, 42, 45].

Although improvements compared to standard $k-\varepsilon$ have been reported using alternative RANS models for in-cylinder flows (e.g., non-linear turbulence models [46, 47]), a comprehensive review of RANS models is beyond the scope of this paper.

Table 1 The constants used in the $k-\varepsilon$ turbulence model

C_μ	σ_k	σ_ε	$C_{\varepsilon1}$	$C_{\varepsilon2}$	$C_{\varepsilon3}$
0.09	1.0	1.22	1.44	1.92	−0.33

4 Results

4.1 Nonswirling Imperial College piston-cylinder assembly

We begin by examining the distribution of the turbulence integral length scale l_0. A rough estimate can be obtained from a RANS run with the $k-\varepsilon$ turbulence model:

$$l_0 = \frac{C_\mu^{0.75} k^{1.5}}{\varepsilon}, \tag{21}$$

where k, ε and C_μ have been defined previously.

To guide the selection of mesh resolution (filter size Δ) for LES, it is useful to examine l_0 and the ratio l_0/Δ. For this configuration, both l_0 and Δ vary with spatial location and with time. Figures 3 and 4 show contours of the integral length l_0 and the ratio l_0/Δ for a 2-D section through the baseline mesh. In Fig. 3 it can be seen that, except in the cells immediately adjacent to the wall and some cells close to the valve, the integral length ranges from 0.3 to 4.8 mm. The integral length scale close to the annular valve is smaller than other locations, which means a finer mesh resolution is required in that region. In Fig. 4 it can be seen for both 36° and 144° after TDC, except in the cells immediately adjacent to the wall and some cells close to the valve, the value of l_0/Δ exceeds unity. As will be shown later, the $k-\varepsilon$ model does not perform particularly well for this configuration, so these length-scale estimates cannot be taken too seriously. Nevertheless, they provide some qualitative guidance. A more direct approach to establish the suitability of the computational mesh is to examine the sensitivity of statistical quantities of interest to variations in mesh size. This analysis is performed below.

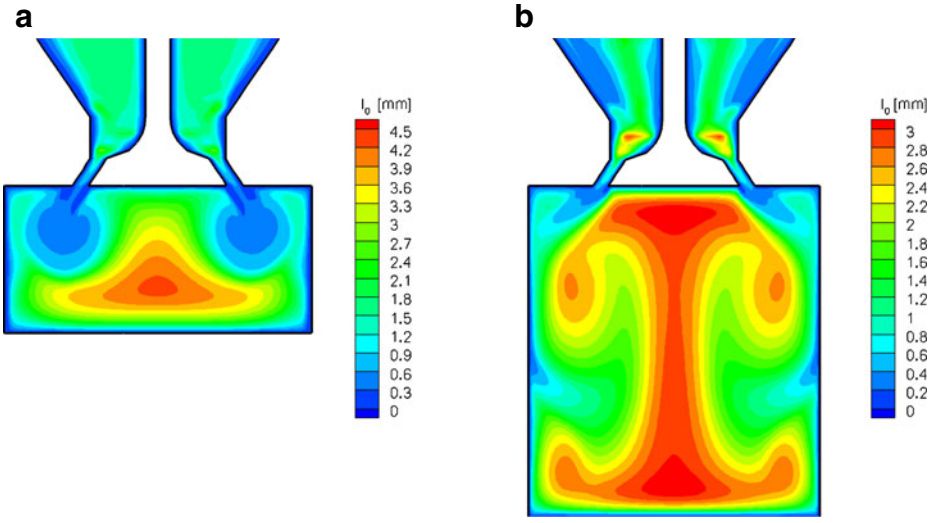

Fig. 3 Contour plot showing the integral length scale l_0 for the baseline mesh. **a** 36° after TDC. **b** 144° after TDC

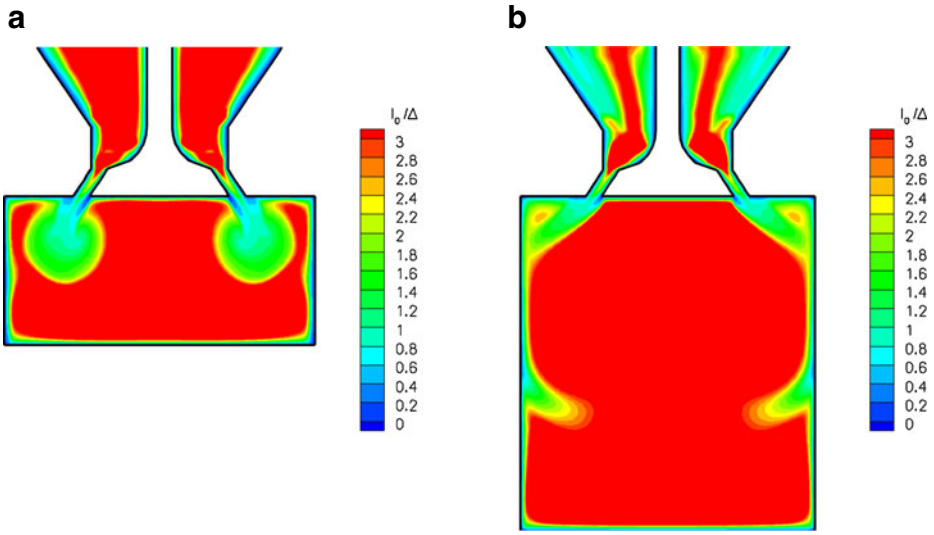

Fig. 4 Contour plot showing the ratio l_0/Δ for the baseline mesh. **a** 36° after TDC. **b** 144° after TDC

As discussed in Section 3.5, for LES calculations without swirl, seven consecutive cycles are simulated and the first two are discarded. The influence of the averaging window is shown in Fig. 5; in all cases, the first two cycles have been discarded. Averaging over three cycles gives results that differ little from those obtained

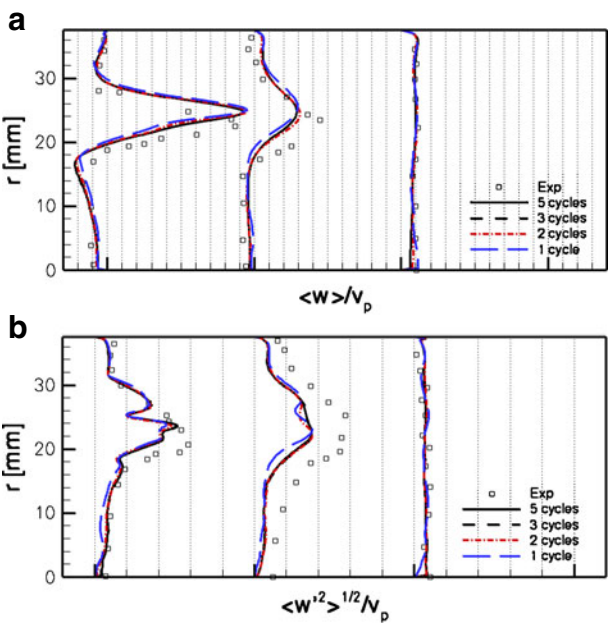

Fig. 5 Computed (*lines*) and measured (*symbols*) radial profiles at 36° after TDC for the baseline case. **a** Mean axial velocity profiles. **b** Axial rms velocity profiles

Table 2 LES run matrix for the nonswirling case

Time step	$\Delta t = 2$ CA	$\Delta t = 1$ CA	$\Delta t = 0.5$ CA	$\Delta t = 0.25$ CA	$\mathbf{\Delta t = 0.1}$ **CA**
Smagorinsky	$C_s = 0.00$	$C_s = 0.01$	$C_s = 0.02$	$C_s = 0.10$	$C_s = 0.20$
SFS model	$C_s = 0.30$	$C_s = 0.50$	$C_s = 0.80$	$C_s = 1.00$	$C_s = 1.50$
One-equation	$C_k = 0.00$	$C_k = 0.01$	$C_k = 0.02$	$C_k = 0.05$	$C_k = 0.10$
SFS model	$C_k = 0.20$	$\boldsymbol{C_k = 0.30}$	$C_k = 0.40$	$C_k = 0.50$	$C_k = 0.80$
Mesh size	Coarse mesh	**Baseline mesh**	Fine mesh		
	170,000 cells	**1,300,000 cells**	2,600,000 cells		

Values in bold font correspond to the baseline case

by averaging over five cycles. This suggests that five cycles are sufficient (even conservative) to ensure converged statistics. In Fig. 5 and subsequent figures, each horizontal tick mark (dashed lines) corresponds to one unit of mean piston speed $\overline{V_p}$. Unless specified otherwise, only the resolved-scale contribution to the rms values is shown. The contribution of the SFS model to rms values will be discussed later.

Table 2 shows the run matrix for the nonswirling case. The parameters in bold font are the baseline parameters. We first show the baseline LES results compared with the measured data. We next compare the RANS and baseline LES results using the same mesh and timestep. Then a parametric sensitivity study is performed where a single parameter is varied at a time with all other parameters remaining at their baseline values.

The computed and measured radial profiles of axial mean and rms velocity with baseline parameters are shown in Figs. 6, 7, 8 and 9. In these figures, only the

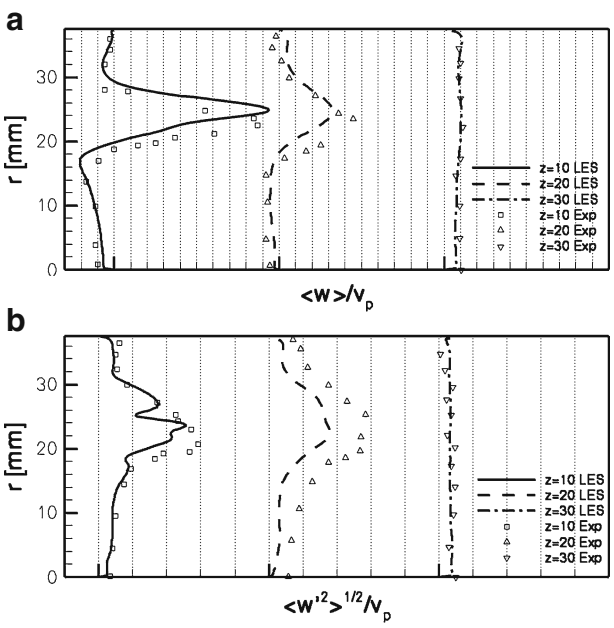

Fig. 6 Computed (*lines*) and measured (*symbols*) radial profiles at 36° after TDC for the baseline case. **a** Mean axial velocity profiles. **b** Axial rms velocity profiles

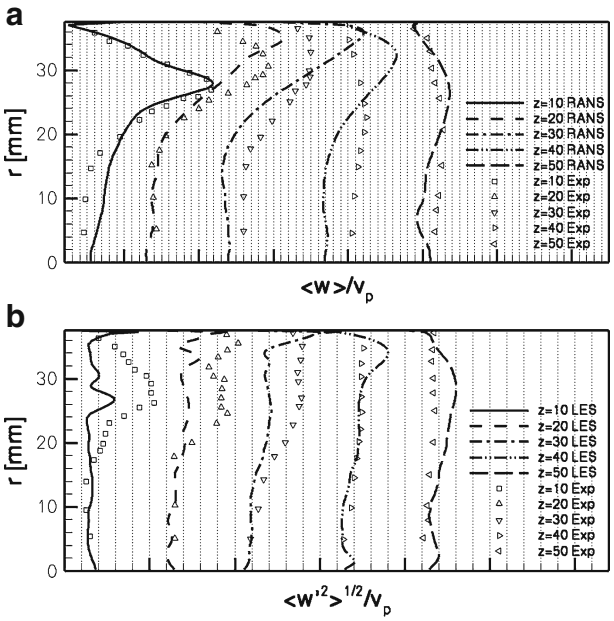

Fig. 7 Computed (*lines*) and measured (*symbols*) radial profiles at 90° after TDC for the baseline case. **a** Mean axial velocity profiles. **b** Axial rms velocity profiles

resolved-scale contribution to the rms values is shown. Figure 6 shows results for three axial stations at 36° after TDC (early on the intake stroke), and Figs. 7–9 show the corresponding results for axial stations at 90°, 144°, and 270° after TDC.

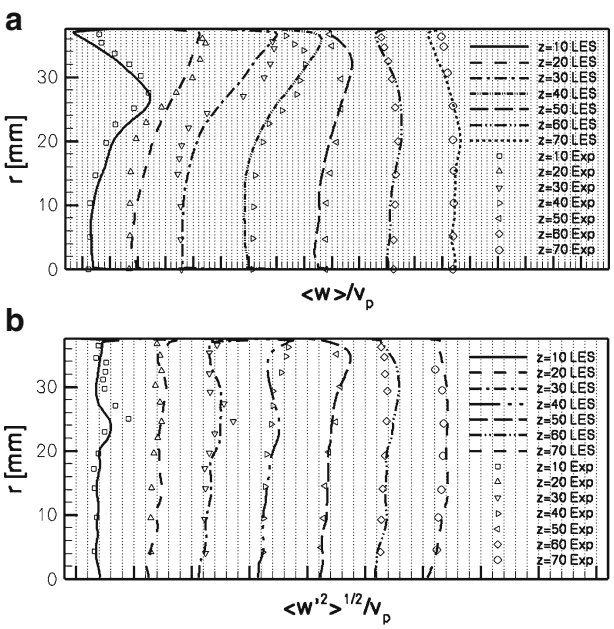

Fig. 8 Computed (*lines*) and measured (*symbols*) radial profiles at 144° after TDC for the baseline case. **a** Mean axial velocity profiles. **b** Axial rms velocity profiles

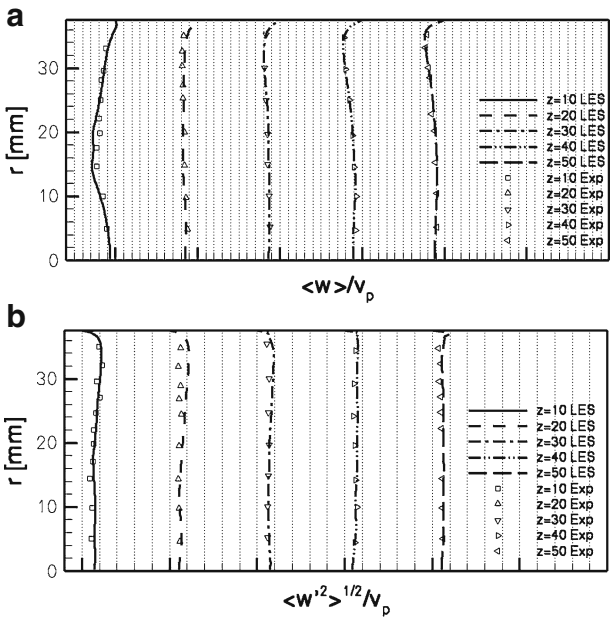

Fig. 9 Computed (*lines*) and measured (*symbols*) radial profiles at 270° after TDC for the baseline case. **a** Mean axial velocity profiles. **b** Axial rms velocity profiles

In general, computed mean velocity profiles are in good agreement with the experimental profiles at 36°, 144° and 270°. The flow undergoes a transition in structure at approximately 90°, and it is difficult to capture the phasing of the transition precisely. Better agreement between model and measurement can be achieved at 90° with different model parameters, but at the expense of poorer agreement at 36° and 144°. Results at 270° are not sensitive to variations in numerical and model parameters and will not be included in the subsequent discussions. The focus will be on the 36° and the 144° results.

The computed rms profile (resolved-scale fluctuations only) at $z = 20$ mm at 36° lies below the experimental profiles. At this measurement location, the local rms velocity is of the same order of magnitude as the local mean velocity. The contribution of the SFS model will be discussed below.

While the agreement between model and measurement is not perfect, both the mean and rms computed profiles show better agreement with measurements than has been reported using any RANS-based model [1, 47], and the present results are similar to those that have been reported in other LES studies for this configuration [2, 3, 23].

4.1.1 Piston motion

As discussed in Section 3.4, there are two different ways to accommodate the moving piston. The first approach is to deform the mesh in the axial direction without layer addition or removal; the second approach involves layer addition and removal in the axial direction without deforming the mesh. Mean axial velocity profiles obtained using the two approaches are compared in Figs. 10 and 11 for a coarse-mesh case.

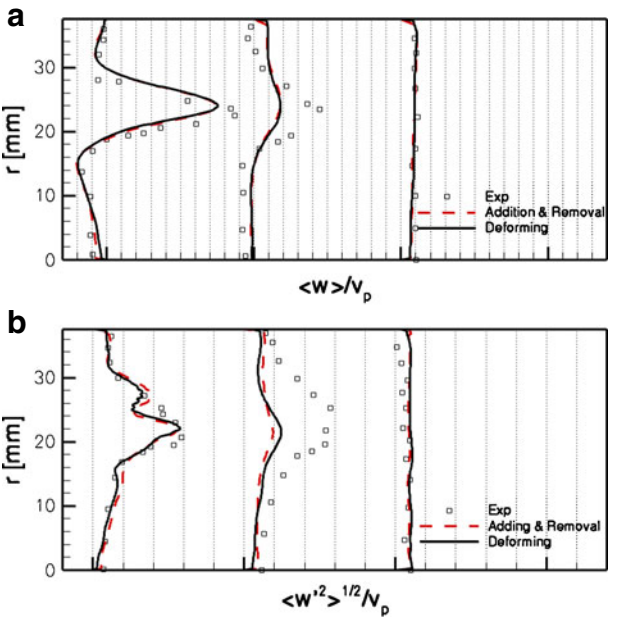

Fig. 10 Computed (*lines*) and measured (*symbols*) radial profiles at 36° after TDC for two approaches to accommodate piston motion. **a** Mean axial velocity profiles. **b** Axial rms velocity profiles

For the first approach, the number of cells is approximately 170,000; for the second approach, the number of cells varies from approximately 70,000–170,000 with the piston movement. It can be seen that the two approaches produce very similar

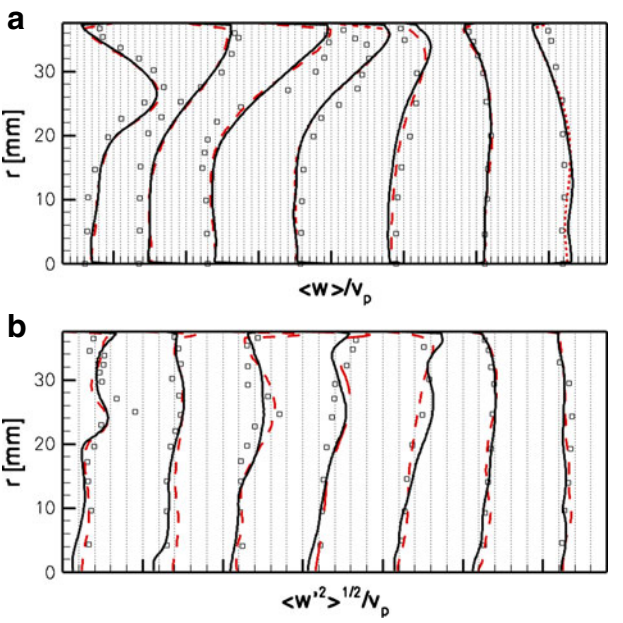

Fig. 11 Computed (*lines*) and measured (*symbols*) radial profiles at 144° after TDC for two approaches to accommodate piston motion. **a** Mean axial velocity profiles. **b** Axial rms velocity profiles

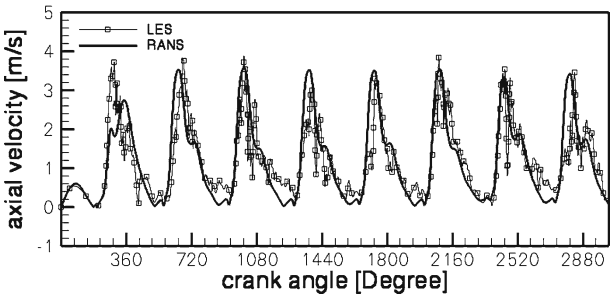

Fig. 12 Computed axial velocity at a fixed spatial location for LES (resolved velocity) and RANS (mean velocity)

results. Unless specified otherwise, all the subsequent results are obtained without cell addition and removal.

4.1.2 RANS vs LES

Baseline LES results are next compared to the results obtained using a standard $k-\varepsilon$ RANS turbulence model with the same mesh and timestep. Figure 12 shows the instantaneous axial velocity component at a fixed spatial location in the cylinder for both LES and RANS. The location is on the center line of the cylinder, approximately 15 mm below the head. After the first two cycles, the RANS mean velocity trace remains essentially the same for subsequent cycles, while significant cycle-to-cycle variations are evident for LES. This figure serves to illustrate a key difference between RANS and LES for in-cylinder flows.

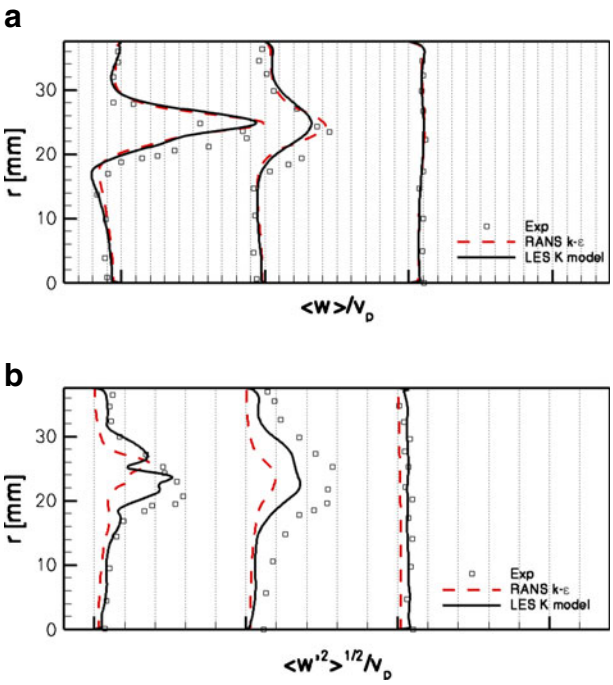

Fig. 13 Computed (*lines*) and measured (*symbols*) radial profiles at 36° after TDC for $k-\varepsilon$ RANS and for the baseline LES case. **a** Mean axial velocity profiles. **b** Axial rms velocity profiles

LES results with baseline parameters are compared with the RANS results in Figs. 13 and 14. For RANS, $\langle w'^2 \rangle^{1/2}$ has been estimated as the square root of $\frac{2}{3}k$, where k is the turbulence kinetic energy. At 36° and 144° after TDC, while the RANS-based mean velocity profiles are at least qualitatively similar to the experimental profiles, the RANS turbulence levels are severely underpredicted.

4.1.3 Sensitivity to grid size

Figures 15 and 16 explore the sensitivity of LES results to variations in the computational mesh (see Table 2). Here the one-equation SFS model with $C_k = 0.3$ and a timestep of 0.1 crankangle degrees have been used. In general, the LES results tend to approach the experimental data as the mesh is refined. Results at $z = 20$ mm, 36° after TDC, in particular improve with the refinement of the mesh. Here only the resolved-scale contribution to the rms velocities is shown.

Establishing the quality of LES results has proven to be difficult. One approach is to consider the resolved-scale and subfilter-scale contributions to the turbulence kinetic energy. Pope [48] and Klein [49] have introduced single-grid estimators of LES quality by estimating the fraction of the residual (subfilter-scale) turbulent kinetic energy in the total kinetic energy. Celik et al. [50] proposed an index of quality for LES based on Richardson extrapolation using multiple meshes. According to Pope [48], a good LES should resolve at least 80% of the turbulence kinetic energy.

The contribution of subfilter-scale velocity fluctuations is shown in Fig. 17b for the baseline mesh at 36° after TDC. Here $\langle w'^2 \rangle^{1/2}_{\mathrm{SFS}}$ has been estimated as the square root of $\frac{2}{3}k_{\mathrm{SFS}}$. At most locations, the subfilter-scale (model) contribution is small

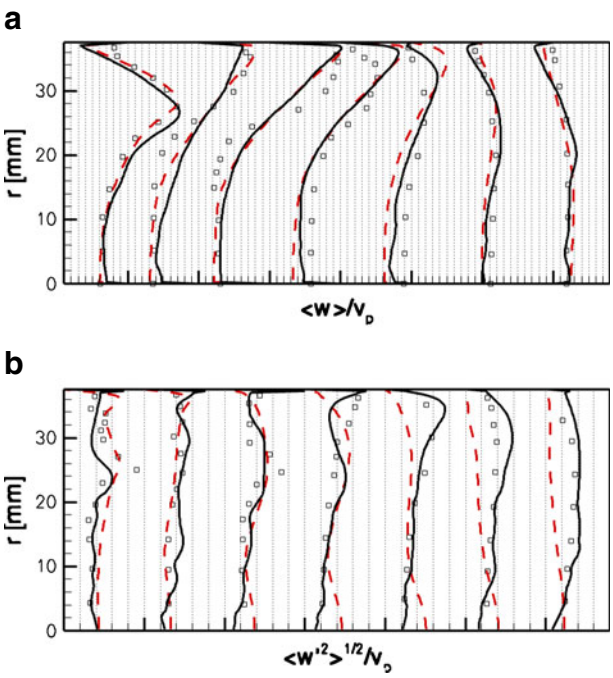

Fig. 14 Computed (*lines*) and measured (*symbols*) radial profiles at 144° after TDC for $k - \varepsilon$ RANS and for the baseline LES case. **a** Mean axial velocity profiles. **b** Axial rms velocity profiles

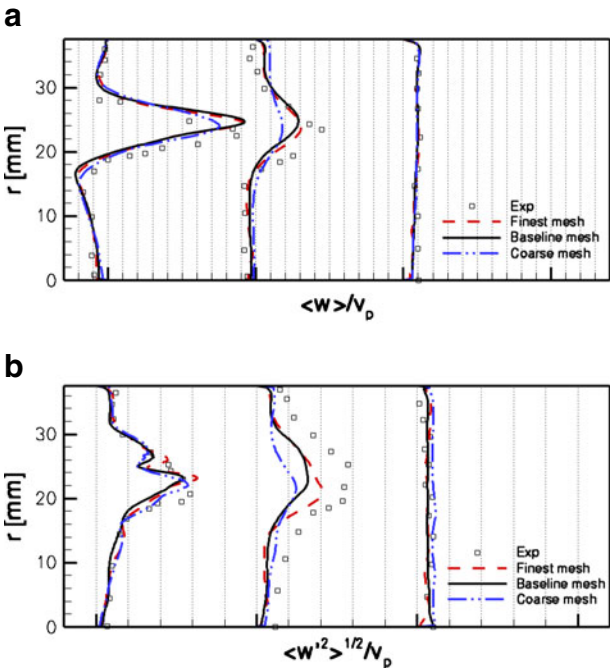

Fig. 15 Computed (*lines*) and measured (*symbols*) radial profiles at 36° after TDC for three meshes. **a** Mean axial velocity profiles. **b** Axial rms velocity profiles

compared to the resolved-scale contribution. At this instant, more than 80% of the TKE is resolved, and a similar conclusion is drawn at the other crankangles (not shown). Figure 17 also shows the sensitivities of the resolved and the model

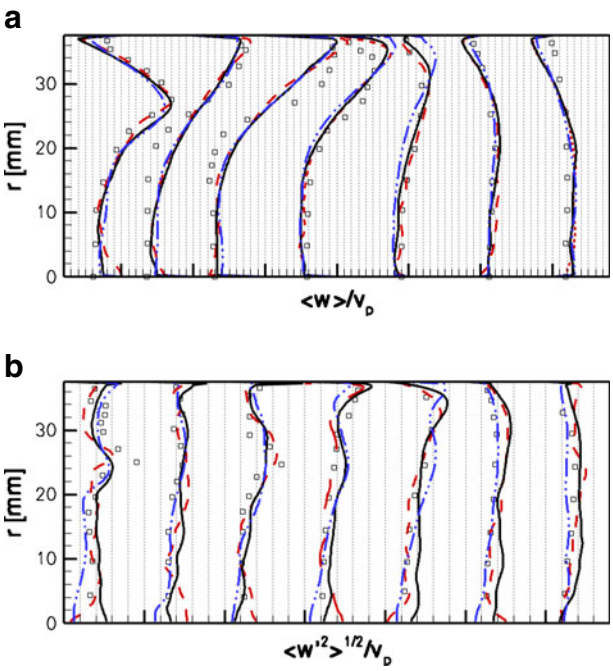

Fig. 16 Computed (*lines*) and measured (*symbols*) radial profiles at 144° after TDC for three meshes. **a** Mean axial velocity profiles. **b** Axial rms velocity profiles

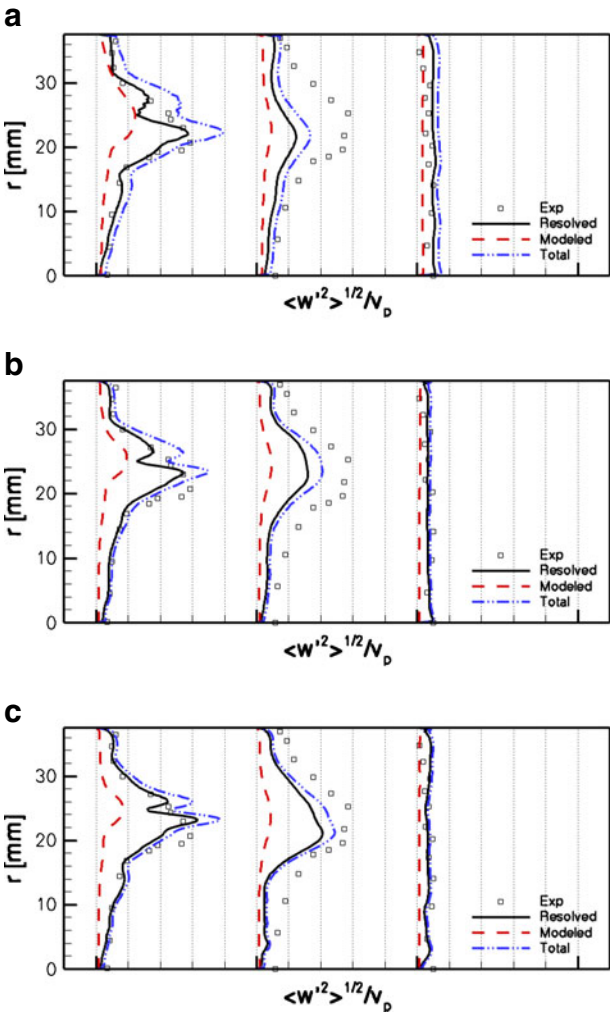

Fig. 17 Computed (*lines*) and measured (*symbols*) radial profiles of axial rms velocity at 36° after TDC. **a** Coarse mesh. **b** Baseline mesh. **c** Fine mesh

contributions to the rms velocity profiles to variations in the mesh size. Compared to the baseline case in Fig. 17b, it can be seen that with the refinement of mesh, the resolved contribution to the rms velocity increases while the SFS model contribution decreases. The sum of the resolved and model contributions increases somewhat from the baseline mesh to the finest mesh, but the increase is small compared to that from the coarse mesh to the baseline mesh. This suggests that the results on the baseline and fine meshes are at least close to being grid independent, in this sense. Similar results are found at 90° and 144° (not shown).

4.1.4 Sensitivity to computational timestep

The influence of computational timestep is examined next. Computed axial mean and rms velocity profiles with different timesteps are shown in Figs. 18 and 19. The baseline timestep of 0.1 crankangle degrees corresponds to a maximum material

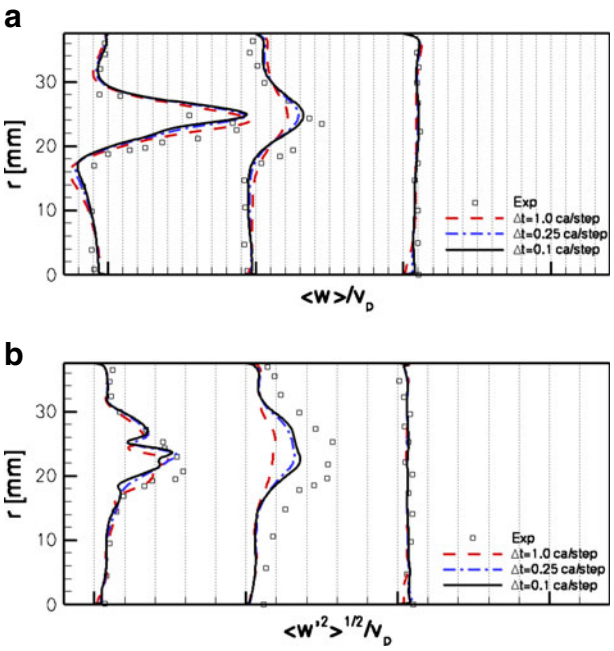

Fig. 18 Computed (*lines*) and measured (*symbols*) radial profiles at 36° after TDC for three computational timesteps. **a** Mean axial velocity profiles. **b** Axial rms velocity profiles

Courant number of approximately 0.033 based on the mean piston speed $\overline{V_p}$. The results are relatively insensitive to timestep provided that the timestep is sufficiently small (here, less than 0.25 crankangle degrees).

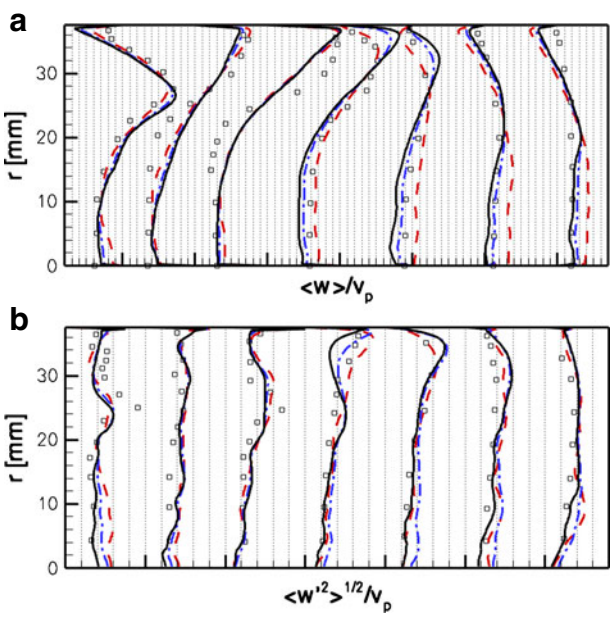

Fig. 19 Computed (*lines*) and measured (*symbols*) radial profiles at 144° after TDC for three computational timesteps. **a** Mean axial velocity profiles. **b** Axial rms velocity profiles

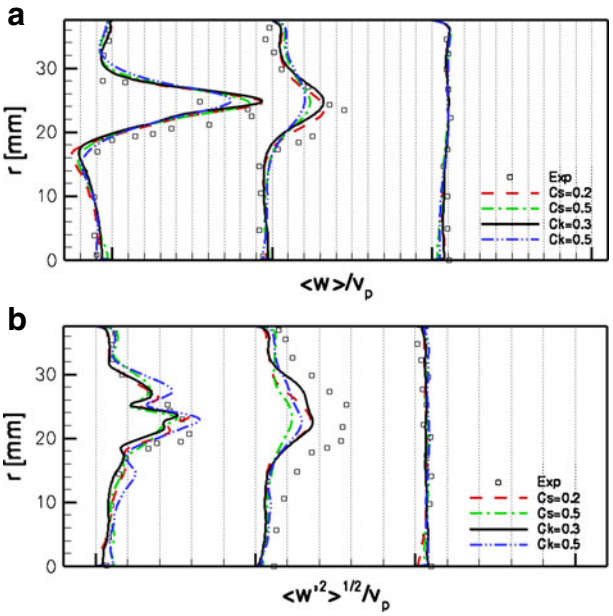

Fig. 20 Computed (*lines*) and measured (*symbols*) radial profiles at 36° after TDC with variations in SFS model. **a** Mean axial velocity profiles. **b** Axial rms velocity profiles

4.1.5 Sensitivity to subfilter-scale models

Figures 20 and 21 show LES results using the Smagorinsky and the one-equation SFS models with different values of the model constants C_s and C_k, respectively. Smaller

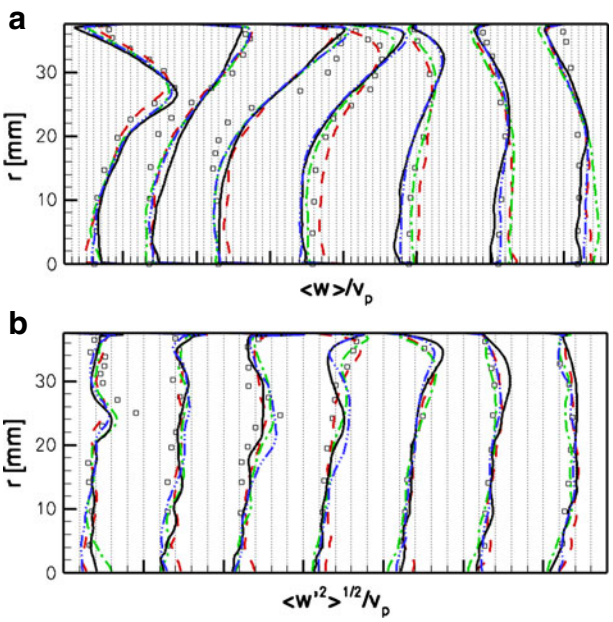

Fig. 21 Computed (*lines*) and measured (*symbols*) radial profiles at 144° after TDC with variations in SFS model. **a** Mean axial velocity profiles. **b** Axial rms velocity profiles

Table 3 LES run matrix for the swirling case

Time step	$\Delta t = 1$ CA	$\mathbf{\Delta t = 0.1}$ **CA**	
Smagorinsky model	$C_s = 0.02$	$C_s = 0.20$	$C_s = 0.30$
One-equation model	$C_k = 0.02$	$\boldsymbol{C_k = 0.05}$	$C_k = 0.10$
Mesh size	Coarse mesh	**Baseline mesh**	
	170,000 nodes	**1,300,000 nodes**	

values of C_s and C_k correspond to smaller apparent turbulence viscosity, and hence to larger resolved-scale rms velocities (higher resolved turbulence level). A wide range of values of C_s and C_k have been tried (Table 2), and the LES results are found to be very sensitive to the subfilter-scale model and its constants. No single value of the model constant gives uniformly the best results for all the locations and crankangles. The cases with $C_s = 0.2$ and $C_k = 0.3$ are found to give the best results overall for the Smagorinsky and one-equation models, respectively. The one-equation SFS model with $C_k = 0.3$ gives slightly better results than that of the Smagorinsky SFS model with $C_s = 0.2$ at the locations shown in Figs. 20 and 21. However, at other crankangles, the Smagorinsky SFS model gives somewhat better results than the one-equation SFS model. The fact that the results are sensitive to variations in the SFS model is encouraging, and suggests that better results might be obtained with more sophisticated SFS models.

4.2 Swirling Imperial College piston-cylinder assembly

A systematic parametric study also has been performed for the swirling case (Table 3). The sensitivities of computed results to variations in physical and numerical parameters are generally similar to those that were observed in the parametric

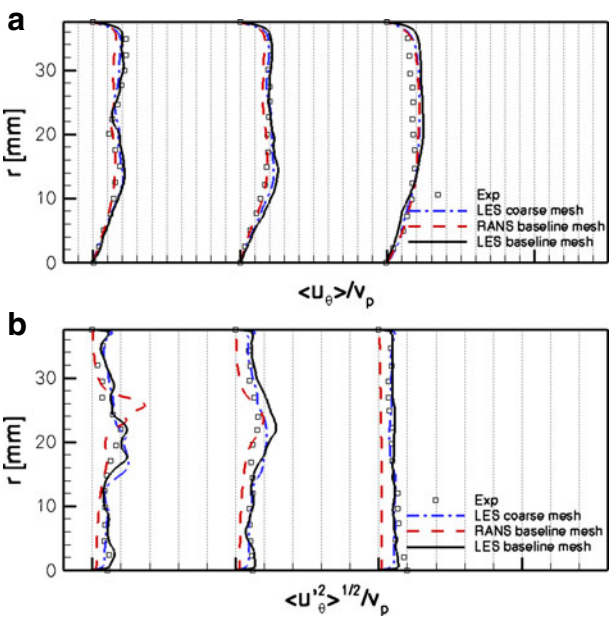

Fig. 22 Computed (*lines*) and measured (*symbols*) radial profiles at 36° after TDC for the swirling case. **a** Mean azimuthal velocity profiles. **b** Azimuthal rms velocity profiles

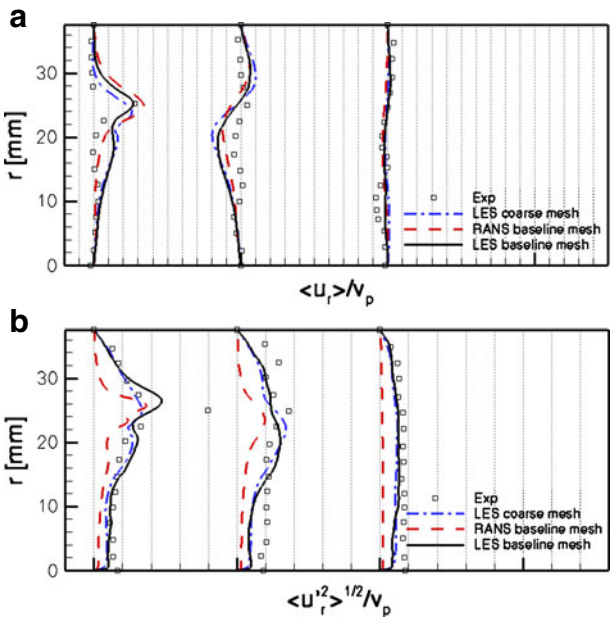

Fig. 23 Computed (*lines*) and measured (*symbols*) radial profiles at 36° after TDC for the swirling case. **a** Mean radial velocity profiles. **b** Radial rms velocity profiles

study for the nonswirling case. Hence the comparisons in this section will be limited to mesh sensitivity and a comparison between LES and RANS with a standard $k - \varepsilon$ turbulence model. The one-equation SFS model with $C_k = 0.05$ gives the best results overall, and that is the value used for all LES results that are shown in this section.

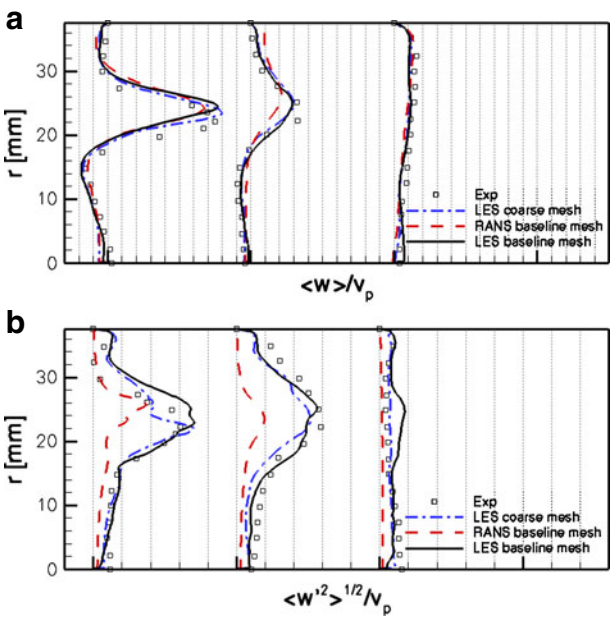

Fig. 24 Computed (*lines*) and measured (*symbols*) radial profiles at 36° after TDC for the swirling case. **a** Mean axial velocity profiles. **b** Axial rms velocity profiles

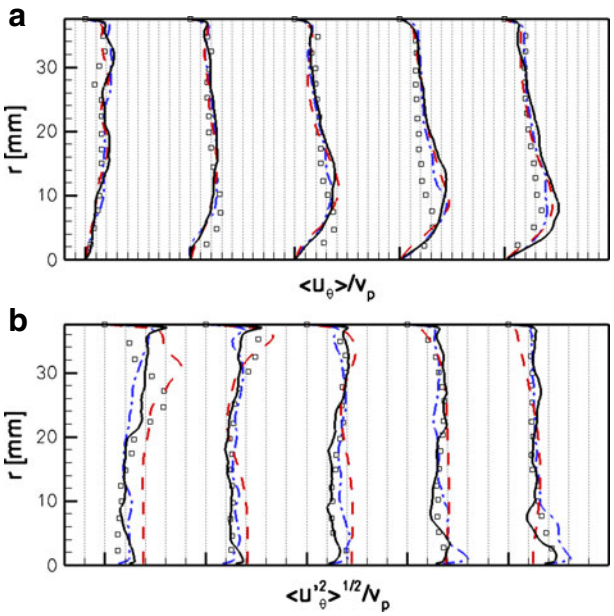

Fig. 25 Computed (*lines*) and measured (*symbols*) radial profiles at 90° after TDC for the swirling case. **a** Mean azimuthal velocity profiles. **b** Azimuthal rms velocity profiles

Figures 22, 23, 24, 25, 26, 27, 28, 29 and 30 show the computed and measured mean and resolved-scale rms profiles of three velocity components at 36°, 90° and 144° after TDC. Because this is the first LES study to be reported for this configuration, LES results are shown for all crankangles at which measurements are available, and for all

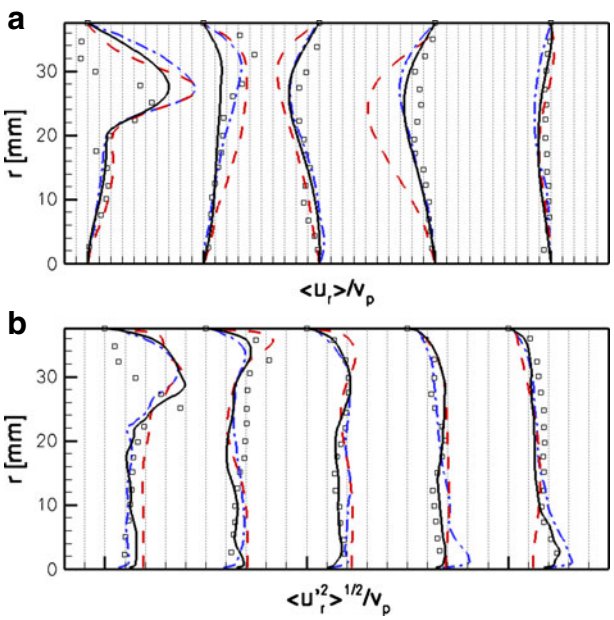

Fig. 26 Computed (*lines*) and measured (*symbols*) radial profiles at 90° after TDC for the swirling case. **a** Mean radial velocity profiles. **b** Radial rms velocity profiles

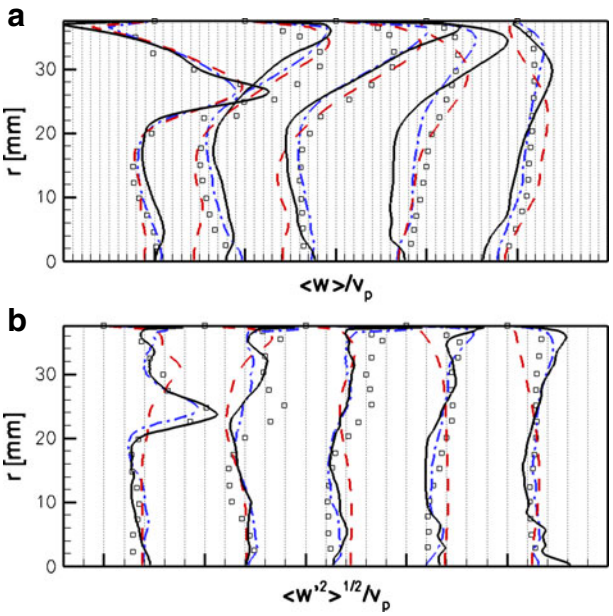

Fig. 27 Computed (*lines*) and measured (*symbols*) radial profiles at 90° after TDC for the swirling case. **a** Mean axial velocity profiles. **b** Axial rms velocity profiles

measurement stations and all three velocity components. For RANS, the rms velocity profiles have been estimated as the square root of $\frac{2}{3}k$, where k is the turbulence kinetic energy.

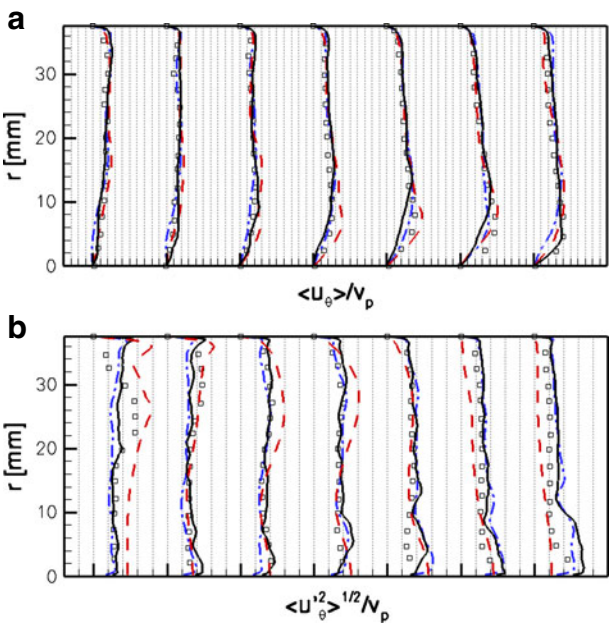

Fig. 28 Computed (*lines*) and measured (*symbols*) radial profiles at 144° after TDC for the swirling case. **a** Mean azimuthal velocity profiles. **b** Azimuthal rms velocity profiles

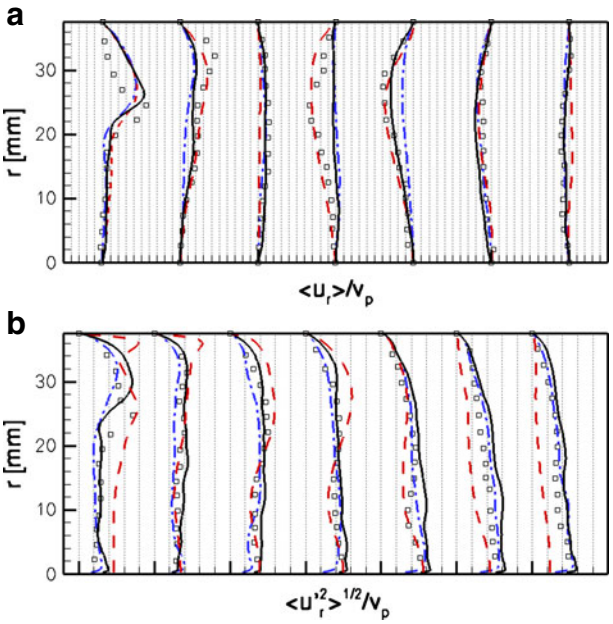

Fig. 29 Computed (*lines*) and measured (*symbols*) radial profiles at 144° after TDC for the swirling case. **a** Mean radial velocity profiles. **b** Radial rms velocity profiles

In general, the LES results are in at least as good agreement with experiment as for the nonswirling cases reported in Section 4.1, and arguably are even better here. For example, the computed and measured axial mean and rms velocity profiles

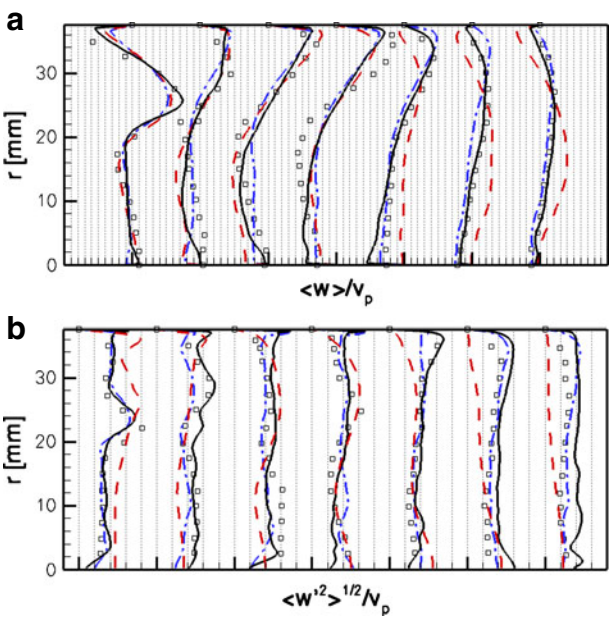

Fig. 30 Computed (*lines*) and measured (*symbols*) radial profiles at 144° after TDC for the swirling case. **a** Mean axial velocity profiles. **b** Axial rms velocity profiles

at 36° and 144° are in better agreement compared to their counterparts for the nonswirling configurations. The LES results again show a significant improvement over the RANS results with $k - \varepsilon$ turbulence model, especially for the rms velocity profiles.

There are important differences in flow structure between the swirling and nonswirling cases; these have been discussed in detail in [20] and [21]. The swirl is far from being solid-body in nature, except close to the cylinder axis (Figs. 22a, 25a and 28a). Compared to the nonswirling case, the mean flow in the configuration with swirl exhibits an elongated main vortex that reaches close to the piston, and a different pattern of secondary vortices. Strong anisotropy is evident in the Reynolds stresses for the swirling case (compare Figs. 22b, 23b and 24b, for example), and the LES captures this quite naturally.

Some discrepancies remain between LES results and experiments, especially at 90°. But overall, these are quite satisfactory results, given the simplicity of the models that have been used and the complexity of this flow.

5 Conclusion

LES has been performed for an axisymmetric piston-cylinder assembly with and without swirl. While several earlier LES studies have been published for the configuration without swirl, these are the first LES results to be reported for the configuration with swirl. For the meshes that have been used in this study, more than 80% of the TKE is resolved, and the amount that is resolved increases as the mesh is refined. The sum of the resolved and modeled contributions to the turbulence kinetic energy approaches grid independence for the meshes that have been used in this study. The sensitivity of LES to key numerical and physical model parameters has been investigated. Results are especially sensitive to mesh and to the SFS turbulence model. Satisfactory results can be obtained using simple viscosity-based SFS turbulence models, although there is room for improvement. No single model gives uniformly best agreement between model and measurements at all measurement stations and crank angles. The strong sensitivity of computed mean and rms velocity profiles to variations in the SFS turbulence model is an encouraging result. This suggests that better results might be obtained using more advanced models, such as dynamic models and/or non-dissipative models [51]. Such models will be explored in future work.

Acknowledgements The authors thank Mr. Navtej Singh, Mr. Erwan Gautier and Dr. Francesca di Mare of CD-adapco for many helpful discussions related to STAR-CD and es-ice. The authors also thank Dr. Tang-wei Kuo and Dr. Shengming Chang of GM R&D Center. The authors gratefully acknowledge financial support from CD-adapco and from the GM R&D Center. The second author is a consultant to CD-adapco.

References

1. El Tahry, S.H., Haworth, D.C.: Directions in turbulence modeling for in-cylinder flows in reciprocating engines. AIAA J. Propuls. Power **8**, 1040–1048 (1992)
2. Haworth, D.C., Jansen, K.: Large-eddy simulation on unstructured deforming meshes: towards reciprocating IC engines. Comput. Fluids **29**, 493–524 (2000)

3. Haworth, D.C.: Large-eddy simulation of in-cylinder flows. In: Oil and Gas Science and Technology, vol. 54, pp. 175–185. Revue de l'Institut Français du Pétrole (1999)
4. Haworth, D.C.: A Review of Turbulent Combustion Modeling for multidimensional In-Cylinder CFD. SAE Paper, no. 2005-01-0993 (2005)
5. Reynolds, W.C.: Computation of turbulent flows. Annu. Rev. Fluid Mech. **8**, 183–208 (1976)
6. Drake, M.C., Haworth, D.C.: Advanced gasoline engine development using optical diagnostic and numerical modeling. In: Proceedings of the Combustion Institute, vol. 31, pp. 99–124 (2007)
7. Celik, I.B., Yavuz, I., Smirnov, A.: Large eddy simulations of in-cylinder turbulence for internal combustion engines: a review. Int. J. Engine Res. **2**(2), 119–148 (2001)
8. Naitoh, K., Itoh, T., Takagi, Y., Kuwahara, K.: Large Eddy Simulation of Premixed-Flame in Engine Based on the Multi-level Formulation and Renormalization Group Theory. SAE Paper, no. 920590 (1992)
9. Celik, I.B., Yavuz, I., Smirnov, A., Smith, J., Amin, E., Gel, A.: Prediction of in-cylinder turbulence for IC engines. Combust. Sci. Technol. **153**(1), 339–368 (2000)
10. Celik, I.B., Amin, E., Smith, J., Yavuz, I., Gel, A.: Towards large eddy simulation using the KIVA-code. In: 11th Intenational Multidimensional Engine Modeling User's Group Meeting. Detroit, Michigan (1998)
11. Amsden, A.A., Ramshaw, J.D., O'Rourke, P.J., Dukowicz, J.K.: KIVA: A Computer Program for Two- and Three-Dimensional Fluid Flows with Chemical Reactions and Fuel Sprays. Tech. Rep. LA-10245-MS, Los Alamos National Laboratory (1985)
12. Smirnov, A., Yavuz, I., Celik, I.B.: Diesel combustion and LES of in-cylinder turbulence for IC engines. In: In-Cylinder Flows and Combustion Processes, ASME Fall Technical Conference. Ann Arbor, Michigan (1999)
13. Smith, J., Smirnov, A., Yavuz, I., Celik, I.B.: Simulation of swirling flows related to an intake stroke of a diesel engine. In: ASME ICE-Division Fall Conference. Clymer, New York (1998)
14. Richard, S., Colin, O., Vermorel, O., Benkenida, A., Angelberger, C., Veynante, D.: Towards large eddy simulation of combustion in spark ignition engines. In: Proceedings of the Combustion Institute, vol. 31, pp. 3059–3066 (2007)
15. Vermorel, O., Richard, S., Colin, O., Angelberger, C., Benkenida, A.: Multi-Cycle LES Simulations of Flow and Combustion in PFI SI 4-Valve Production Engine. SAE Paper, no. 2007-01-0151 (2007)
16. Goryntsev, D., Sadiki, A., Klein, M., Janicka, J.: Large eddy simulation based analysis of the effects of cycle-to-cycle variations on air-fuel mixing in realistic DISI ic-engines. In: Proceedings of the Combustion Institute, vol. 32, pp. 2759–2766 (2009)
17. Banerjee, S., Liang, T., Rutland, C.J., Hu, B.: Validation of an LES Multi Mode Combustion Model for Diesel Combustion. SAE Paper, no. 2010-01-0361 (2010)
18. Angelberger, C.: LES for Internal Combustion Engine Flows (Rueil-Malmaison, France), IFP, 1–2 December 2008. See http://www.ifp.com
19. Morse, A., Whitelaw, J.H., Yianneskis, M.: Turbulent Flow Measurement by Laser–Doppler Anemometry in a Motored Reciprocating Engine. Tech. Rep. FS/78/24, Imperial College Department of Mechanical Enginnering (1978)
20. Morse, A., Whitelaw, J.H., Yianneskis, M.: The Influence of Swirl on the Flow Characteristics of a Reciprocating Piston-Cylinder Assembly. Tech. Rep. FS/78/41, Imperial College Department of Mechanical Enginnering (1978)
21. Morse, A., Whitelaw, J.H., Yianneskis, M.: The influence of swirl on the flow characteristics of a reciprocating piston-cylinder assembly. J. Fluids Eng. **102**, 478–480 (1980)
22. Morse, A., Whitelaw, J.H., Yianneskis, M.: Turbulent flow measurement by Laser–Doppler anemometry in a motored piston-cylinder engine. J. Fluids Eng. **101**, 208–216 (1979)
23. Verzicco, R., Mohd-Yusof, J., Orlandi, P., Haworth, D.C.: Large eddy simulation in complex geometric configuration using boundary body forces. AIAA J. **38**, 427–433 (2000)
24. El Tahry, S.H.: A comparison of three turbulence models in engine like geometries. In: Proceedings of International Symposium on Diagnostics and Modeling of Combustion in Reciprocating Engines: COMODIA 85 (Tokyo, Japan), pp. 203–213 (1985)
25. Pope, S.B.: Turbulent Flows. Cambridge University Press, Cambridge (2000)
26. Germano, M.: A proposal for redefinition of the turbulent stresses in the filtered Navier–Stokes equations. Phys. Fluids **29**(7), 2323–2324 (1986)
27. Germano, M.: Turbulence: the filtering approach. J. Fluid Mech. **238**, 325–336 (1992)
28. Smagorinsky, J.: General circulation experiments with the primitive equations. Mon. Weather Rev. **91**(3), 99–164 (1963)
29. Peyret, R.: Handbook of Computational Fluid Dynamics. Academic, London (2000)

30. Lilly, D.K.: The representation of small-scale turbulence in numerical simulation experiments. In: IBM Science and Computing Symposium on Environmental Science (Yorktown Heights, New York, USA) (1967)
31. Di Mare, F.: Large eddy simulation of reacting and non-reacting turbulent flows in complex geometries. PhD thesis, University of London (2002)
32. Piomelli, U., Chasnov, J.R.: Large-Eddy Simulations: Theory and Applications, vol. 7. Kluwer Academic, Dordrecht (1996)
33. Deardorff, J.W.: On the magnitude of the sub grid scale eddy coefficient. J. Comput. Phys. **7**, 120–133 (1970)
34. Yoshizawa, A.: Statistical theory for compressible turbulent shear flows, with the application to subgrid scale modeling. Phys. Fluids **29**, 2152–2164 (1986)
35. Speziale, C.G.: Analytical methods for the development of Reynolds-stress closures in turbulence. Annu. Rev. Fluid Mech. **23**, 107–157 (1991)
36. Horiuti, K.: A proper velocity scale for modelling subgrid-scale eddy viscosities in large eddy simulation. Phys. Fluids A **5**, 146–157 (1992)
37. Yoshizawa, A.: A statistically derived subgrid model for the large eddy simulations of turbulence. Phys. Fluids **25**, 1532–1538 (1982)
38. Spalding, D.B.: A single formula for the law of the wall. J. Appl. Mech. **28**, 455–458 (1961)
39. CD-adapco: Methodology for STAR-CD VERSION 4.06 (2008)
40. Issa, R.I.: Solution of the implicitly discretised fluid flow equations by operator-splitting. J. Comput. Phys. **62**, 40–65 (1986)
41. CD-adapco: User Guide for STAR-CD VERSION 4.06 (2008)
42. Launder, B.E., Spalding, D.B.: The numerical computation of turbulent flows. Comput. Methods Appl. Mech. Eng. **3**, 269–289 (1974)
43. Rodi, W.: Influence of buoyancy and rotation on equations for the turbulent length scale. In: Proceedings of the Second Symposium On Turbulent Shear Flows (Imperial College, London), pp. 10.37–10.42 (1979)
44. El Tahry, S.H.: $k - \varepsilon$ equation for compressible reciprocating engine flows. AIAA J. Energy **7**(4), 345–353 (1983)
45. Kim, S.-E., Choudhury, D.: A near-wall treatment using wall functions sensitized to pressure gradient. In: ASME, FED, vol. 217 (1995)
46. Miles, P.C., Rempel Ewert, B.H., Reitz, R.D.: Experimental assessment of a non-linear turbulent stress relation in a complex reciprocating engine flow. In: 14th Int Symp on Applications of Laser Techniques to Fluid Mechanics (Lisbon, Portugal) (2008)
47. Son, C.H., Shethaji, T.A., Rutland, C.J., Barths, H., Lippert, A., El Tahry, S.H.: Application of non-linear turbulence models in an engine-type flow configuration. Int. J. Engine Res. **8**(5), 449–464 (2007)
48. Pope, S.B.: Ten questions concerning the large-eddy simulation of turbulent flows. New J. Physics **6**(35), 1–24 (2004)
49. Klein, M.: An attempt to assess the quality of large eddy simulation in the context of implicit filtering. Flow Turbul. Combust. **75**, 131–147 (2005)
50. Celik, I.B., Cehreli, Z.N., Yavuz, I.: Index of resolution quality for large eddy simulation. J. Fluids Eng. **127**(5), 949–958 (2005)
51. Chumakov, S., Rutland, C.J.: Dynamic structure models for scalar flux and dissipation in large eddy simulation. AIAA J. **42**(6), 1132–1139 (2004)